SAND2018-10892

SANDIA REPORT

Unlimited Release
Printed Sept. 2018

Coupled Magnetic Spin Dynamics and Molecular Dynamics in a Massively Parallel Framework: LDRD Final Report

Julien Tranchida, Mitchell A. Wood, Stan G. Moore

Prepared by
Sandia National Laboratories
Albuquerque, New Mexico 87185 and Livermore, California 94550

Sandia National Laboratories is a multimission laboratory managed and operated by National Technology & Engineering Solutions of Sandia, LLC, a wholly owned subsidiary of Honeywell International Inc., for the U.S. Department of Energys National Nuclear Security Administration under contract DE-NA0003525.

Sandia National Laboratories

Issued by Sandia National Laboratories, operated for the United States Department of Energy by Sandia Corporation.

Available to DOE and DOE contractors from
U.S. Department of Energy
Office of Scientific and Technical Information
P.O. Box 62
Oak Ridge, TN 37831

Telephone: (865) 576-8401
Facsimile: (865) 576-5728
E-Mail: reports@adonis.osti.gov
Online ordering: http://www.osti.gov/bridge

Available to the public from
U.S. Department of Commerce
National Technical Information Service
5285 Port Royal Rd
Springfield, VA 22161

Telephone: (800) 553-6847
Facsimile: (703) 605-6900
E-Mail: orders@ntis.fedworld.gov
Online ordering: http://www.ntis.gov/help/ordermethods.asp?loc=7-4-0#online

Unlimited Release
Printed Sept. 2018

Coupled Magnetic Spin Dynamics and Molecular Dynamics in a Massively Parallel Framework: LDRD Final Report

Julien Tranchida, Mitchell A. Wood, Stan G. Moore
Multiscale Science Dept.
Sandia National Laboratories
P.O. Box 5800, Albuquerque, NM 87185-1322
jtranch@sandia.gov

Abstract

This report summarizes the result of the LDRD Exploratory Express project 211666-01, titled "Coupled Magnetic Spin Dynamics and Molecular Dynamics in a Massively Parallel Framework".

Acknowledgment

The authors would like to warmly thank their manager Veena Tikare, Aidan Thompson, and Steve Plimpton for their support and help through the crafting of the proposal and during the studies involved in this LDRD. The authors would also like to thank Attila Cangi for providing support and help with the spin-dependent density functional theory calculations, and for performing the density of state calculations presented in the Appendix.

This work was funded by the Exploratory Express (LDRD) Program at Sandia National Laboratories, Project Number 211666 and Title "Coupled Magnetic Spin Dynamics and Molecular Dynamics in a Massively Parallel Framework".

Sandia National Laboratories is a multimission laboratory managed and operated by National Technology & Engineering Solutions of Sandia, LLC, a wholly owned subsidiary of Honeywell International Inc., for the U.S. Department of Energy's National Nuclear Security Administration under contract DE-NA0003525.

This paper describes objective technical results and analysis. Any subjective views or opinions that might be expressed in the paper do not necessarily represent the views of the U.S. Department of Energy or the United States Government.

Contents

Summary

This work aimed at developing the first computational capability of its kind. Integrated within Sandia's LAMMPS code, the numerical tool presented in this report enables the simulation of coupled magnetic and mechanic phenomena with previously unachievable fidelity and scale. Sandia researchers will now be able to deeply understand and exploit these phenomena for predictions of advanced functional materials, in applications such as remote sensing, quantum computing, or energy devices.

This page intentionally left blank.

Chapter 1

Introduction and Motivation

Two standard methodologies for numerical studies of magnetic and mechanical properties of materials are spin dynamics (SD) and molecular dynamics (MD), respectively [1, 2]. Both methods simulate materials at the atomic level, modeling electron-mediated interactions and integrating the equations of motion of the spins/atoms. Standard MD simulations can directly simulate a material containing $> 10^9$ atoms, or equivalently $\approx 1\,\mu m^3$ on modern leadership computing platforms. The coupling of SD and MD enables simulations of coupled lattice and magnetic degrees of freedom, making it possible to tackle a broad range of phenomena related to magneto-elasticity [3]. Early studies have revealed very promising results. Notable examples are the influence of vacancy formation on the ferromagnetism of BCC iron, and simulations of magneto-caloric effects [4, 5, 6].

However, very few research groups have implemented this coupled methodology, and existing SD-MD codes are impeded by at least four strong restrictions:

- their level of parallelization is very limited, which prevents the simulation of large magnetic systems [7],
- none of them has been released as part of an open source, commonly used MD code, which is preventing Sandia researchers from adopting this method [8], and from a larger user-base to grow and develop new potentials,
- those implementations lack physical models accounting for the spin-orbit coupling (SOC), which is essential to simulate magneto-elasticity [9],
- none of them account for the long-range magnetic dipolar interaction, which is fundamental to stabilize magnetic domains that play a key role in magnetic materials.

An initial SD-MD package is currently being developed at Sandia in the LAMMPS code [10], and already overcomes the two first restrictions. The lack of the last two points still prevents from performing device-level simulations needed at Sandia. Developing and implementing them are the two key improvements that will come out of this work. For the long-range interaction, an Ewald summation technique exists in LAMMPS. However, this method, only implemented for electrical dipoles, scales very poorly with the number of particles and is not suitable for large-scale simulations. Another method, known as particle-particle particle-mesh (P3M), will be added. Relying on fast Fourier transforms, P3M scales

much better while still accurately modeling the long-range interactions. Simultaneously, new terms accounting for SOC will be developed and implemented. In order to ensure accurate predictions for a given material, the SOC model must be parameterized from ab initio techniques such as density functional theory. Early feedback from Sandia experimentalists has identified iron, cobalt and iron-cobalt alloys as useful materials for this model development. Test simulations that can be directly compared to experimental results will be designed at each step in this process.

Chapter 2

Initial Release into LAMMPS of a Symplectic and Scalable Algorithm for Coupled Spin Dynamics and Molecular Dynamics

The initial step in this project consisted in releasing an open source package to allow scalable coupled spin dynamics and molecular dynamics calculations. To this end, an initial package, referred to as SPIN, was released in LAMMPS. The associated source files can be found within LAMMPS, in the following directory : `lammps/src/SPIN`. All the technical details associated to this implementation were presented in an article published in Journal of Computational Physics [11].

From `lammps/src`, LAMMPS can be built with the SPIN package by typing the following commands :

```
$ make yes-spin # add the SPIN package to LAMMPS
$ make serial   # build a serial LAMMPS executable
$ make mpi      # build a parallel LAMMPS executable with MPI
```

We refer to the LAMMPS documention pages for more information on how to build LAMMPS.

A documentation on how to use this package was added to the LAMMPS documentation. In `lammps/examples/SPIN`, a set of examples were provided. They provide the input to run simple spin-lattice calculations of magnetic transition metals (iron, cobalt and nickel), or to use other functionalities, such as the read/restart options.

The release of this package embedded within LAMMPS provides a broad scientific community and Sandia researchers with an open-source, scalable implementation of SD-MD. The following chapters of this report present two ongoing improvements of this initial development, that will both be released into LAMMPS as part of the SPIN package.

This page intentionally left blank.

Chapter 3

Implementation of Ewald Sums and P3M for Long-Range SD-MD Simulations

The functional properties of magnetic materials are known to result from a combination of short- and long-range interactions. Local magnetic alignment, induced by the exchange interaction or by the magnetocrystalline anisotropy, can usually be accounted for by short-range (or even ultra-local) models. They allow the SD-MD framework to scale as order $O(N)$ (with N the number of simulated particles). The initial SPIN package released into LAMMPS accounts for most of the usual magnetic short-range interactions.

When larger magnetic configurations are simulated, magnetic domains and domain walls can become a fundamental feature and even define the properties of the simulated magnetic devices. The stabilization, or even nucleation, of magnetic domain configurations usually requires accounting for the magnetic dipolar interaction. As the energy associated to the dipolar interaction decays as $1/r^3$, it has to be treated as a long-range interaction [12]. When long-range interactions are taken into account in an MD or SD-MD formalism, a direct calculation of the associated forces and energy scales as $O(N^2)$ and quickly becomes computationally intractable for all but the smallest simulations.

In order to reduce this computational cost, spectral methodologies relying on accounting for periodic virtual images of the simulation cell have been developed. In this section, we present how two of those methodologies, referred to as Ewald sums and P3M, can be applied to the simulation of magnetic dipolar interactions. The Ewald sum cost scales at best as $O(N^{3/2})$ and at worst as $O(N^2)$. P3M cost scales as $O(N \log N)$, making it computationally feasible for very large systems.

The expressions of the energy and forces associated to the magnetic dipolar interaction are first provided. Then we describe the two implemented methodologies. Finally, a description of the methods used to verify correctness of the implementation along with preliminary numerical results probing the scaling.

Magnetic Dipolar Energy and Forces

The magnetic dipolar energy can be expressed as :

$$\mathcal{H}_{\text{dipolar}} = -\frac{\mu_0 \left(\mu_B\right)^2}{4\pi} \sum_{i,j,i\neq j}^{N} \frac{g_i g_j}{r_{ij}^3} \left[3(\boldsymbol{e}_{ij} \cdot \boldsymbol{s}_i)(\boldsymbol{e}_{ij} \cdot \boldsymbol{s}_j) - \boldsymbol{s}_i \cdot \boldsymbol{s}_j\right] \tag{3.1}$$

with $\mu_0 = 4\pi \cdot 10^{-7}$ T m A^{-1} the vacuum permeability and $\mu_B \approx 5.788 \cdot 10^{-5}$ eV T^{-1} the Bohr magneton. For two sites i and j, $\boldsymbol{e}_{ij}$ is the unit vector pointing from i to j, the inter-atomic distance is denoted r_{ij}, $\boldsymbol{s}_i$ and $\boldsymbol{s}_j$ are two unit vectors giving the direction of the atomic magnetic spins, and g_i and g_j are their associated Lande factors.

As discussed in the introduction, the magnetic dipolar energy corresponds to a long-range potential. Therefore, in general, the sums in eq. (3.1) are not restricted to a given radius cutoff, but apply to all spins present in the system.

From the energy provided by eq. (3.1) and by applying a spin-lattice Poisson bracket as presented in Appendix A, the associated equations of motion (EOM) can be derived. For a given spin i, this derivation gives a magnetic precession vector $\boldsymbol{\omega}_i$:

$$\boldsymbol{\omega}_i = \frac{\mu_0 (\mu_B)^2}{4\pi\hbar} \sum_j \frac{g_i g_j}{r_{ij}^3} \Big(3\left(\boldsymbol{e}_{ij} \cdot \boldsymbol{s}_j\right)\boldsymbol{e}_{ij} - \boldsymbol{s}_j\Big) \tag{3.2}$$

and a mechanical force $\boldsymbol{F}_i$:

$$\boldsymbol{F}_i = \frac{\mu_0 (\mu_B)^2}{4\pi} \sum_j \frac{g_i g_j}{r_{ij}^4} \Big[\Big((\boldsymbol{s}_i \cdot \boldsymbol{s}_j) - 5(\boldsymbol{e}_{ij} \cdot \boldsymbol{s}_i)(\boldsymbol{e}_{ij} \cdot \boldsymbol{s}_j)\Big)\boldsymbol{e}_{ij} + (\boldsymbol{e}_{ij} \cdot \boldsymbol{s}_i)\boldsymbol{s}_j + (\boldsymbol{e}_{ij} \cdot \boldsymbol{s}_j)\boldsymbol{s}_i\Big] \tag{3.3}$$

The mechanical stress generated by the force given by eq. (3.3) is probably negligible in most materials. However, its effects can be fundamental for other types of magnetic simulations (such as the simulation of magnetic particles in suspension in a fluid). Therefore, we decided to include its computation within our framework.

Ewald Sums and P3M Methods

For periodic three-dimensional systems, the Ewald and P3M methods can be considered to account for the magnetic dipolar interaction. The very basic idea of both methodologies is based on the following decomposition :

$$\frac{1}{r^3} = \frac{\text{erf}(\alpha r)}{r^3} + \frac{\text{erfc}(\alpha r)}{r^3} \tag{3.4}$$

where $1/r^3$ schematically represents the dipolar energy given by eq. (3.1), and α is referred to as a splitting parameter, which defines the mutual influence of the two terms in the

right-hand side of eq. (3.4). The erfc component in eq. (3.4) is rapidly decaying, and is therefore evaluated as a short-range interaction in the real-space. On the other hand, the erf component is containing most of the long-range effects, and is computed in the reciprocal-space by generating virtual periodic images of the simulation cell. The two methodologies presented here (Ewald and P3M) only differ on how they evaluate this reciprocal-space component.

Applying this decomposition to the dipolar energy, eq. (3.1) can be recasted into the following sum :

$$\mathcal{H}_{\text{dipolar}} = \mathcal{H}^r_{\text{dipolar}} + \mathcal{H}^k_{\text{dipolar}} + \mathcal{H}^s_{\text{dipolar}} \tag{3.5}$$

where $\mathcal{H}^r_{\text{dipolar}}$ and $\mathcal{H}^k_{\text{dipolar}}$ are the real- and reciprocal space components respectively, and $\mathcal{H}^s_{\text{dipolar}}$ is a self-interaction correction (as the reciprocal-space component accounts for an interaction of each particle with itself). According to refs. [13, 14], these three different terms can be expressed as follows :

$$\mathcal{H}^r_{\text{dipolar}} = \frac{\mu_0 \left(\mu_B\right)^2}{4\pi} \sum_{i,j,i\neq j}^{N} \frac{g_i g_j}{r_{ij}^3} \Big[g_1(r_{ij}) \left(\boldsymbol{s}_i \cdot \boldsymbol{s}_j\right) - 3\, g_2(r_{ij}) \left(\boldsymbol{e}_{ij} \cdot \boldsymbol{s}_i\right) \left(\boldsymbol{e}_{ij} \cdot \boldsymbol{s}_j\right) \Big] \tag{3.6}$$

$$\mathcal{H}^k_{\text{dipolar}} = \frac{\mu_0 \left(\mu_B\right)^2}{4\pi\, L^3} \sum_{\boldsymbol{k}\neq 0} \frac{4\pi}{k^2} \exp\left[-\left(\frac{\pi k}{\alpha L}\right)^2 \right] \sum_{i,j=1}^{N} g_i g_j \left(\boldsymbol{k} \cdot \boldsymbol{s}_i\right) \left(\boldsymbol{k} \cdot \boldsymbol{s}_j\right) \exp\left(\frac{2\pi i \boldsymbol{k} \cdot \boldsymbol{r}_{ij}}{L}\right) \tag{3.7}$$

$$\mathcal{H}^s_{\text{dipolar}} = -\frac{2\alpha^3}{3\sqrt{\pi}} \sum_{i=1}^{N} \boldsymbol{s}_i^2 \tag{3.8}$$

with $g_1(r_{ij})$ and $g_2(r_{ij})$ defining two radial functions such as:

$$g_1(r_{ij}) = \frac{\operatorname{erfc}(\alpha r_{ij})}{r_{ij}^3} + \frac{2\alpha}{\sqrt{\pi} r_{ij}^2}\, e^{-(\alpha r_{ij})^2} \tag{3.9}$$

$$g_2(r_{ij}) = \frac{\operatorname{erfc}(\alpha r_{ij})}{r_{ij}^3} + \frac{1}{\sqrt{\pi}} \left(\frac{4\alpha^3}{3} + \frac{2\alpha}{r_{ij}^2}\right) e^{-(\alpha r_{ij})^2} \tag{3.10}$$

and $k = |\boldsymbol{k}|$ with $\boldsymbol{k}$ denoting a vector of the reciprocal-space.

Note that the real-space term defined by eq. (3.6) is evaluated up to a given radius cutoff r_c, and is assumed to be negligible beyond this cutoff (which is consistent with the rapid decay of the erfc function).

The computation of the reciprocal space term defined by eq. (3.7) involves the resolution of a Poisson equation [15], such as :

$$-\boldsymbol{\nabla}\phi(\boldsymbol{r}) = 4\pi \boldsymbol{\rho}\left(\boldsymbol{r}\right) \tag{3.11}$$

where $\phi(\boldsymbol{r})$ is a magnetostatic potential and $\boldsymbol{\rho}(\boldsymbol{r})$ a spin density function [16]. In practice, the resolution of this Poisson equation is performed in the reciprocal-space, as the differentiation becomes trivial [15]. The two methodologies (Ewald and P3M) mainly differ by the way they evaluate this spin density function, which will have a strong influence on the numerical tools that can be used to solve the above Poisson equation, as detailed below. In simple Ewald sums, one has the following definition for $\boldsymbol{\rho}(\boldsymbol{r})$:

$$\boldsymbol{\rho}(\boldsymbol{r}) = \sum_{i=1}^{N} \delta(\boldsymbol{r} - \boldsymbol{r}_i)\ \boldsymbol{s}_i \tag{3.12}$$

with $\boldsymbol{r} \in V$, and $\delta(\boldsymbol{r} - \boldsymbol{r}_i)$ denoting the Dirac δ function. In the P3M methodology, a mesh M is created and superposed to the simulation cell prior to the evaluation of the real-space density. Then, the on-mesh spin density function $\boldsymbol{\rho}_m(\boldsymbol{r}_m)$ is defined as :

$$\boldsymbol{\rho}_m(\boldsymbol{r}_m) = \sum_{i=1}^{N} W(\boldsymbol{r}_m - \boldsymbol{r}_i)\ \boldsymbol{s}_i \tag{3.13}$$

where $W(\boldsymbol{r}_m - \boldsymbol{r}_i)$ is an assignment function whose definition and tabulation can be found in refs. [17] and [18].

When performing the reciprocal-space resolution of the Poisson equation, the reciprocal spin density function needs to be evaluated first. Within the Ewald framework, the reciprocal spin density has to be computed by the application of a Fourier transform, and one has :

$$\hat{\boldsymbol{\rho}}(\boldsymbol{k}) = \mathrm{FT}\{\boldsymbol{\rho}(\mathrm{r})\}. \tag{3.14}$$

The scaling of this FT is $O(N^2)$ in the general case. Even if the choice of an appropriate splitting factor can reduce the cost of the overall operation to $O(N^{3/2})$, it remains extremely costly for large simulations.

On the other hand, the definition of an on-mesh spin density function allows the P3M methodology to use Fast-Fourier-Transform (FFT) routines. One has :

$$\hat{\boldsymbol{\rho}}_m(\boldsymbol{k}) = \mathrm{FFT}\{\boldsymbol{\rho}_{\mathrm{m}}(\mathrm{r_m})\}. \tag{3.15}$$

This greatly improves the scaling of the calculation, which drops down to $O(N \log N)$, making simulations of large systems much more tractable.

Finally, we also note that corrections of the Ewald and P3M methodologies accounting for two-dimensional slab geometries were also implemented [19].

The two methodologies were implemented into LAMMPS, and the associated source files can be found in the following repositories : `lammps/src/SPIN` and `lammps/src/KSPACE` (the routines evaluating the short-range real-space components are part of the SPIN package, whereas the routines evaluating the Ewald and P3M reciprocal-space components are parts of the KSPACE repository). Those new implemented routines were documented, and illustrative examples of how to use them can be found in `lammps/examples/SPIN/pppm_spin/`.

Verification and Scaling Tests

In order to verify the new P3M long-range solver for dipoles was implemented correctly, a system of two interacting dipoles was used. Values for the energy, forces, and torques from P3M were compared to two reference calculations: the first was a highly-refined Ewald sum, and the second was a direct pair-wise calculation with an extremely large cutoff. The error estimator for P3M was then verified using 100 dipoles placed randomly in a cubic box, and the error in the P3M forces was compared to a highly refined Ewald sum to obtain true and estimated force errors.

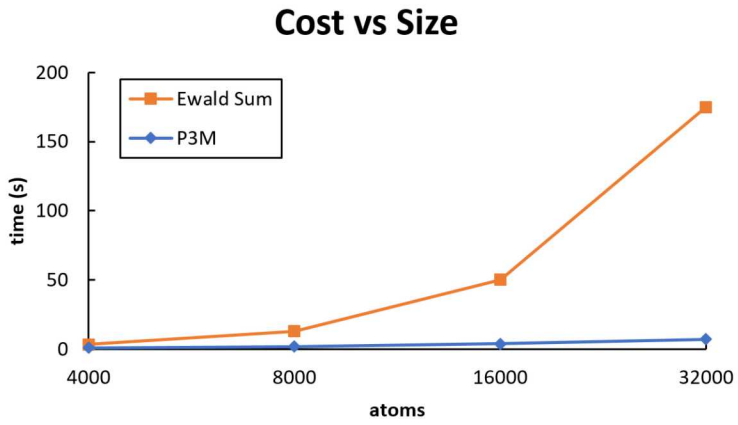

Figure 3.1: Cost of Ewald vs P3M for increasing system size on a single CPU core.

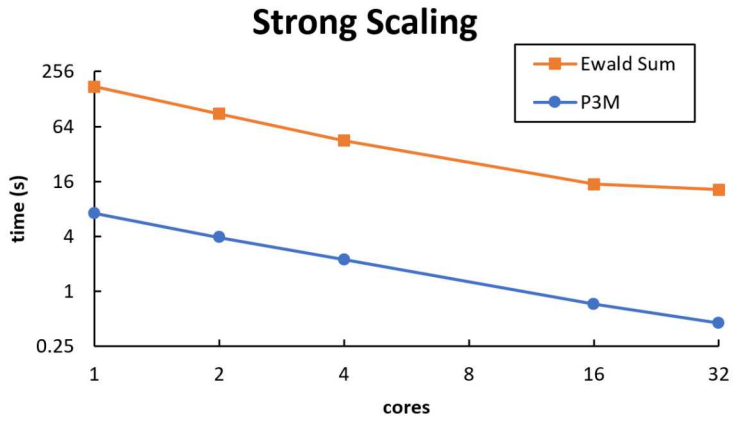

Figure 3.2: Time vs number of CPU cores for 32K dipoles.

As shown in Figure 3.1, the cost of P3M vs an Ewald sum was compared for 4K to 32K dipoles distributed on an face-centerd cubic lattice using a relative force accuracy metric of 10^{-4}. P3M is much faster than an Ewald sum for large systems due to its superior $O(N \log N)$ scaling. The parallel scalability of P3M was also checked by strong-scaling a 32K dipole system from 1 to 32 CPU cores on a single Intel Haswell node. As shown in Figure 3.2, P3M strong scales well up to 32 cores for this system size.

This page intentionally left blank.

Chapter 4

Development of Magneto-Elastic Interactions Accounting for the SOC Effects in HCP Crystals

In this chapter, a numerical model accounting for effects of the SOC is presented. To this end, two well-known magnetic effects arising from the SOC are studied: the magnetocrystalline anisotropy and the magnetostriction. The magnetocrystalline anisotropy corresponds to the presense of prefered axis for the magnetization in magnetic crystals. It strongly depends on the symmetries of the crystal at stake. The magnetostriction corresponds to a generated stress in response to a change of the magnetization orientation, or, on the contrary, to a change of the magnetization orientation in response to a directional stress.

Our study focused on hcp crystals. Two reasons justified this choice. The first one is that the Néel pair interaction has already proven to be a good candidate for the simulation of both the magnetostriction and the magnetocrystalline anisotropy in hcp crystals [20, 21]. Therefore, we hope to build on these former studies and develop a more accurate magnetostriction model than previously achieved, which can be used for large scale magneto-elastic simulations. Besides, this pair interaction is well-suited for an implementation in a coupled SD-MD code, and it depends on radial functions (see in the following section) which can be parametrized to match *ab initio* or experimental results. The second reason is that two very common ferromagnetic materials, cobalt and gadolinium, have hcp lattices at room temperature, and are known to exhibit strong SOC effects. Cobalt is a very common ferromagnetic material, and is used as a component of numerous magnetic devices. Gadolinium is currently being studied as a potential candidate for magneto-caloric devices. Therefore, developing the numerical capability of performing sufficiently accurate simulations of those two materials is of practical relevance for researchers at Sandia and in other DOE laboratories.

In this work, the parametrization of the Néel pair interaction was performed using *ab initio* calculations.

In the first section of this chapter, the fundamental equations associated to the Néel pair anisotropy are recalled. The second section summarizes how spin-dependent density functional theory accounting for the SOC effects was used to compute the magnetostriction in hcp cobalt. Finally, the expression of the magnetostriction is related to the Néel pair interaction and a fit of the numerical *ab initio* results is presented.

Definition of the Néel Pair Anisotropy

The Néel pair anisotropy is represented by a pair interaction which couples the lattice with the direction of magnetization. It was initially developed by Néel to simultaneously reproduce both magnetostrive and anisotropic effects [20].

For a given site i, the interaction can be expressed as the following sum over the first neighbors labeled j, such as:

$$\mathcal{H}_{N\acute{e}el} = -\sum_{i,j}^{N} g\left(r_{ij}\right)\left(\cos(\phi)^2 - \frac{1}{3}\right) + q\left(r_{ij}\right)\left(\cos(\phi)^4 - \frac{30}{35}\cos(\phi)^2 + \frac{3}{35}\right), \tag{4.1}$$

with $g(r_{ij})$ and $q(r_{ij})$ two radial functions of the interatomic distance r_{ij}, and ϕ the angle between the magnetization vector $\boldsymbol{s}$ and $\boldsymbol{e}_{ij} \equiv (\boldsymbol{r}_i - \boldsymbol{r}_j)/|\boldsymbol{r}_i - \boldsymbol{r}_j|^2$, the normalized vector connecting site i and j, and ϕ the defined as :

$$\cos(\phi) = \boldsymbol{s} \cdot \boldsymbol{e}_{ij}, \tag{4.2}$$

where the magnetization vector $\boldsymbol{s}$ is defined as a global averaged quantity, being the same for every magnetic spin. This first definition is convenient for the magnetostriction calculations and parametrizations presented in the next sections of this chapter. However, it is not suitable for an SD-MD definition, where the orientation of neighboring spins can vary and differ due to thermal effects, or antisymmetric interactions. In this case, eq. (4.1) can be recast into :

$$\begin{aligned}\mathcal{H}_{N\acute{e}el} &= -\sum_{i,j}^{N} g_1(r_{ij})\left((\boldsymbol{e}_{ij}\cdot\boldsymbol{s}_i)(\boldsymbol{e}_{ij}\cdot\boldsymbol{s}_j) - \frac{\boldsymbol{s}_i\cdot\boldsymbol{s}_j}{3}\right) + q_1(r_{ij})\left((\boldsymbol{e}_{ij}\cdot\boldsymbol{s}_i)^2 - \frac{\boldsymbol{s}_i\cdot\boldsymbol{s}_j}{3}\right)^2 \\ &+ q_2(r_{ij})\Big((\boldsymbol{e}_{ij}\cdot\boldsymbol{s}_i)(\boldsymbol{e}_{ij}\cdot\boldsymbol{s}_j)^3 + (\boldsymbol{e}_{ij}\cdot\boldsymbol{s}_j)(\boldsymbol{e}_{ij}\cdot\boldsymbol{s}_i)^3\Big)\end{aligned} \tag{4.3}$$

with :

$$g_1\left(r_{ij}\right) = g\left(r_{ij}\right) + \frac{12}{35}q\left(r_{ij}\right) \tag{4.4}$$

$$q_1\left(r_{ij}\right) = \frac{9}{5}q\left(r_{ij}\right) \tag{4.5}$$

$$q_2\left(r_{ij}\right) = -\frac{2}{5}q\left(r_{ij}\right) \tag{4.6}$$

This interaction was implemented as part of the SPIN package and the associated source files can be found in the following repository : `lammps/src/SPIN`. This interaction was documented in the LAMMPS documentation, and an example of how to use it can be found in `lammps/exampls/SPIN/hcp_cobalt`.

In the next sections of this chapter, a methodology for the parametrization of this interaction for cobalt is presented.

Spin-Dependent DFT Calculations

The strength of the spin-orbit coupling for a particular material is highly sensitive to the local environment around each atom-centered spin. An example of this sensitivity is the large lattice strains that are imposed by a change in external magnetic field. In a classical MD simulation, the equations of motion of each atom is propagated by calculating forces from a Born-Oppenheimer potential energy surface called an interatomic potential, or just potential for short. For the present work, these potentials need to be adapted by adding an extra energy (and forces when differentiated) term that corresponds to the magnetic degrees of freedom. The base potential that we are using for Cobalt uses the Embedded Atom Model (EAM) developed by Foiles *et. al.* [22] and the specific parameter set used here is taken from Pun *et. al.* [23]. Simpler, but still effective, potentials formulate the energy of an atomic configuration that is solely based on a sum pair-wise interactions between atoms. We aim to develop a simple pair-wise functional that only captures the spin-orbit interactions and subsequently add this to the existing EAM potential for Cobalt.

In order to translate the analytical form of the spin-orbit coupling in equation 4.1 into a form compatible with LAMMPS a set of DFT calculations is needed to construct a database of energies to constrain the fitted $g(r_{ij})$ and $q(r_{ij})$ functions to. This section will detail how this DFT database is constructed and how a fit was optimized. Since the focus is on crystalline Cobalt in the HCP phase, a DFT code using a plane wave basis is optimal and the Vienna Ab initio Simulation Package (VASP) is used here [24, 25, 26]. Each of these training geometries was calculated with a 15 x 15 x 15 Monkhorst Pack k-point mesh, 600eV plane wave cutoff energy, 0.1eV Gaussian smearing, PBE exchange-correlation functional [27] and a GW pseudopotential that captures core electrons leaving the outermost d- and s-orbitals for the basis set. A convergence test on the number of k-points and energy cutoff was performed to arrive at these final values. Calculations were performed using the orthorhombic unit cell containing four atoms. Within VASP there are three different treatments of the magnetic state of the material, the simplest being the non-magnetic solution. While the non-magnetic solution is not interesting to this work, these calculations were initially performed as a sanity check on the subsequent magnetic calculations performed. The other two treatments of the magnetic state within VASP are known as the collinear and non-collinear solutions. Collinear solutions to a spin-polarized calculation are that of freely rotating spins but spin-orbit interactions are not included. Conversely, spin-polarized calculations that include spin-orbit interactions are categorized as non-collinear solutions. Therefore, the energy difference between these two types of calculations is the energy associated with the spin-orbit coupling.

While DFT is a powerful *ab initio* tool for studying materials physics, certain approximations need to be made. These approximations fall into two categories, those made on the physical model and those related to ease of computation. The main approximations within DFT come down to the choice of pseudopotential and exchange-correlation functional, the former being mainly a computational convenience and the latter an approximate physical model. Also the theory that underlies DFT does not universally capture strongly correlated electron effects, f-electron shells are examples of this shortcoming. Due to these approximations, it is not guaranteed that a well done DFT calculation will match with known

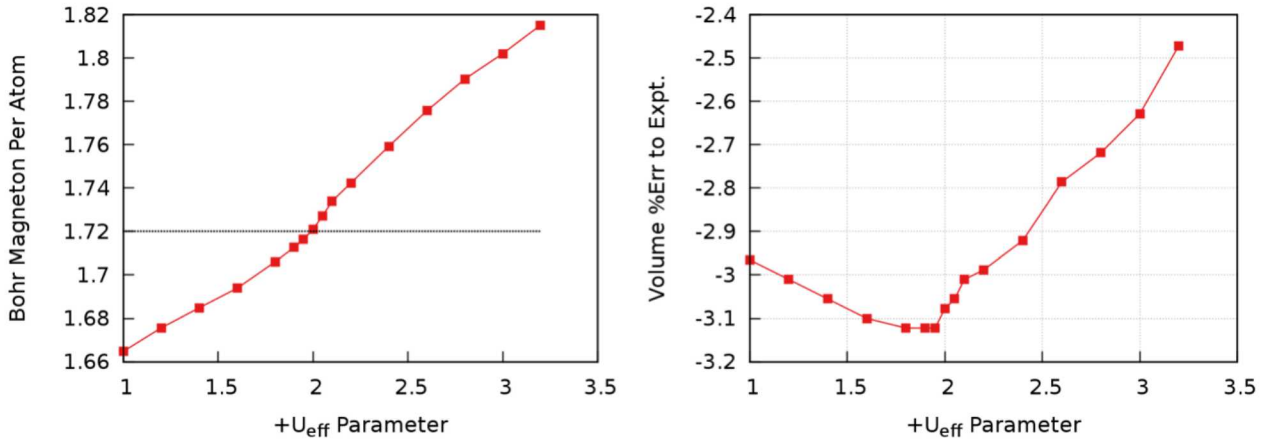

Figure 4.1: **(Left)** Variation of the Bohr magneton per Cobalt atom calculated using VASP with a Hubbard on-site correction applied to d-electrons. Dashed horizontal line at 1.72 indicated the experimental prediction that this calculation aimed to match. **(Right)** Relaxed cell volume prediction with respect to experiment as the +U correction is varied. A PBE-GGA exchange and correlation functional is used in these calculations, a discrepancy of a few percent in cell volume is to be expected using DFT regardless of XC functional used.

experimental quantities. In the present work an additional, but adjustable, approximation is needed in order to make our DFT calculations agree with the experimentally observed Bohr magneton per atom in Cobalt. Here we have opted for the use of the Hubbard on-site correction term in the style of Dudarev *et. al.* [28] and have only applied this correction term to the d-electrons in the calculation. The Hubbard on-site correction, or simply called the +U correction, is an extra energy penalty on electrons that biases the solution toward fully occupied or unoccupied bands. In the VASP implementation of Dudarev's approach, there are two adjustable scalar parameters (U and J), but only the difference between them enters the energy penalty expression. Therefore, we leave $J = 0$ and only optimize U in order to reproduce the experimentally observed Bohr magneton per atom of 1.72. With increasing U there is a monotonic increase in the Bohr magneton per atom, but the relaxed cell volume has a minima just below $U = 2.0eV$, these results are presented in Figure 4.1. From this we settle on $U = 1.95eV$ as the Hubbard screening strength for all subsequent spin-polarized calculations, this includes collinear and non-collinear states.

Following the derivations of Mason [29] the magnetosriction of an HCP material can be calculated given a set deformations on the lattice. Each deformation that Mason identifies also has a corresponding spin polarization. We have carried out VASP calculations that match these conditions for both collinear and non-collinear spin states. An example of one of these calculations is shown in Figure 4.2 wherein each spin in the unit cell is initialized in the direction of its nearest neighbor in the basal plane and the cell is expanded (strain greater than one) and contracted (strain less than one) along this spin direction. What is clear from this figure is that both calculations, with and without spin-orbit coupling, have very similar energy changes due to this elastic deformation. Furthermore, the energy difference between

them is on the order of tens of meV/atom, or equivalently less than one-percent strain in this direction. The strain on the lattice is varied over a very large range in order to properly sample a set of interatomic distances needed for fitting the continuous SOC energy functions ($g(r_{ij})$ and $q(r_{ij})$) for use in MD. In truth, any set of DFT calculations that sample the spin orbit energy landscape as a function of interatomic distance can be used, we decided to reproduce Mason's theoretical derivation for a later validation of our MD predictions, see Appendix B for more details. One of the main concerns with following Mason's method for calculating the magnetostriction is the ad hoc way that VASP defines the initial spin state. Physically, if the spin state deviates from its preferred axis (perpendicular to the basal plane in HCP) it is due to the presence of an external magnetic field. However, VASP does not have the capability to perform calculations in the presence of an external field. Additional calculations were needed in order to confirm that the initial spin states that Mason proposes are physically realizable without the need of a strong magnetic field. Here we define 'strong' as the field strength needed to cause significant population change between the up and down spin channels. To evaluate this, we launched a set of simulations using the Elk electronic structure code [30] which has the capability to study the spin sate of a material in the presence of an external magnetic field. Our local Elk expert, Attila Cangi of 1444, reproduced the VASP results using the Hubbard +U term, and then set out to determine the field strengths need to cause significant changes in the electronic structure. For a spin state perpendicular to the easy axis in HCP Co, the VASP predicted energy change is on the order of 10meV. In contrast, the Elk calculations find that (details in Appendix C) the Zeeman energy threshold to see significant changes in the spin-polarized band structure is greater than 4eV or equivalently $4.7 \cdot 10^5$ Tesla. This result gives confidence that the VASP calculations mimicking Mason's derivation are physically reasonable since the energy scale difference between spin polarizations is significantly smaller than the onset of field induced changes in the band structure.

The last step in defining the spin-orbit interactions in MD comes down to fitting the $g(r_{ij})$ and $q(r_{ij})$ functions of the Néel interaction Hamiltonian. In principle these two functions are empirical and can be any functional form that is continuous in r_{ij}, but also goes to zero as the atom separation goes to infinity. The second of these requirements, locality of the spin-orbit interaction, is needed to maintain efficient calculation (order N) as the size of the simulated system grows. In the present work we decided to use a a polynomial expansion up to order four to fit both $g(r_{ij})$ and $q(r_{ij})$, with switching functions applied to both the short-range($< 1.0\mathring{A}$) and long-range($> 4.0\mathring{A}$) interactions.

$$g(r) = a_0 + \sum_{i=1}^{4} a_i \cdot (r - r_0)^i \tag{4.7}$$

$$q(r) = b_0 + \sum_{i=1}^{4} b_i \cdot (r - r_0)^i \tag{4.8}$$

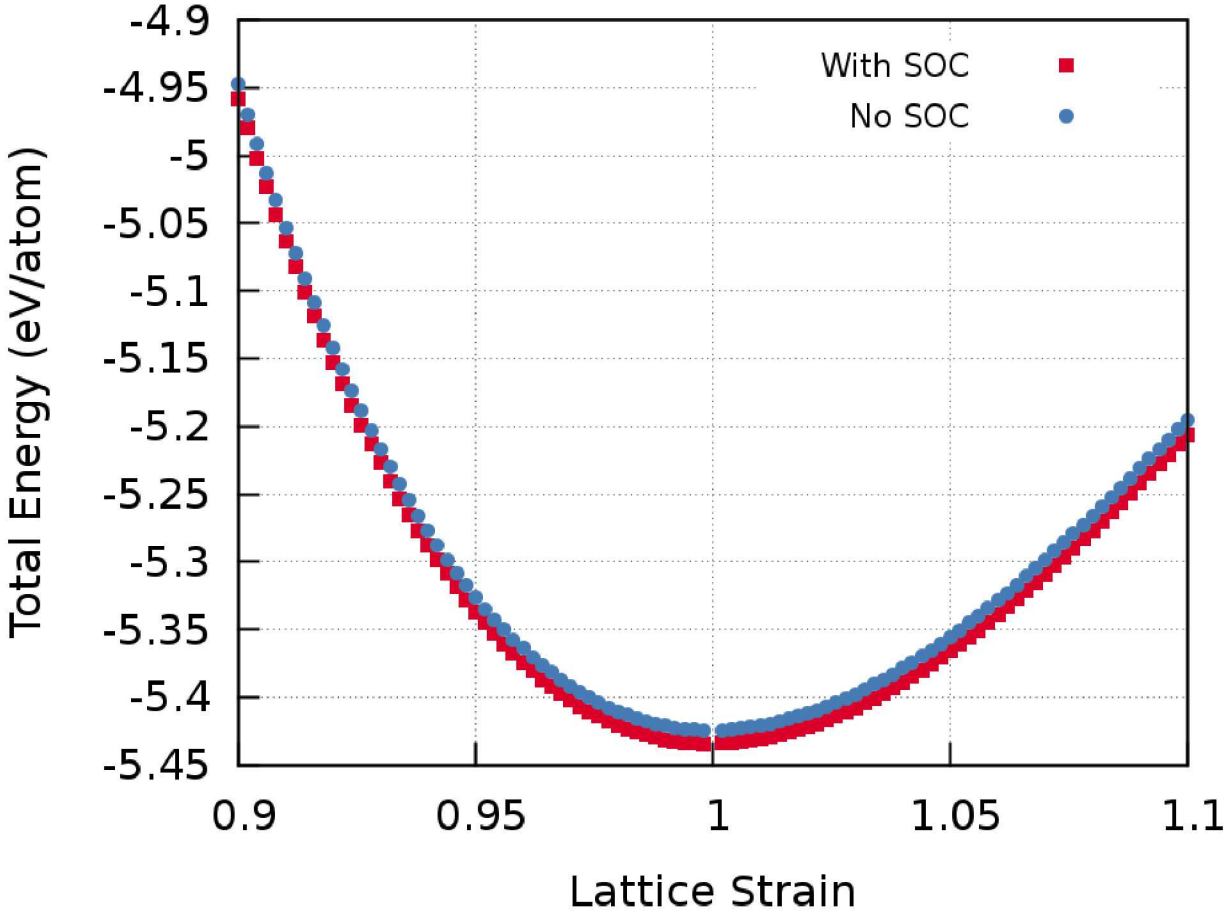

Figure 4.2: VASP calculations mimicking the first of Mason's analytical expressions for magnetostriction in HCP metals. The simulation cell is varied along the nearest neighbor direction in the basal plane in both a compressive and tensile distortion. While most of the energy change is due to the deformation, the remaining difference between the collinear (blue points) and non-collinear (red points) is the energy contribution of the spin-orbit coupling.

The switching functions are defined as :

$$s_{\text{short}} = \begin{cases} 0.0 & r \leq r_{\text{short}} - \Delta r \\ \left(1 - \sin\left(\frac{\pi(r - r_{\text{short}})}{2\Delta r}\right)\right)/2 & |r - r_{\text{short}}| \leq \Delta r \\ 1.0 & r \geq r_{\text{short}} + \Delta r \end{cases} \tag{4.9}$$

and :

$$s_{\text{long}} = \begin{cases} 1.0 & r \leq r_{\text{long}} - \Delta r \\ \left(1 - \sin\left(\frac{\pi(r - r_{\text{long}})}{2\Delta r}\right)\right)/2 & |r - r_{\text{long}}| \leq \Delta r \\ 0.0 & r \geq r_{\text{long}} + \Delta r \end{cases} \tag{4.10}$$

with $r_{\text{short}} = 1.0\mathring{A}$, $r_{\text{long}} = 4.0\mathring{A}$, and $\Delta r = 1.0\mathring{A}$. Those functions will smoothly taper the dipolar and quadrupolar functions to zero, with the added benefit that the derivatives are continuous as well. The free parameters in equation 4.8 are each of the a_i, b_i and r_0 meaning the fit has eleven free variables to minimize the regression error on. To efficiently solve for the optimal parameter set, and to avoid local minima in this overdetermined fit, a genetic algorithm within DAKOTA [31] is used. After one-hundred generations of three-hundred candidates each, an optimal set of parameters was achieved with the mean absolute error of $0.0031eV$. The resultant fitted functions are plotted in Figure 4.3 wherein the Dipolar ($g(r_{ij})$), Quadrapolar ($q(r_{ij})$) and their summation are shown. The summation of these two spin-orbit interactions shows a minima very close to the nearest neighbor distance in the equilibrium HCP crystal.

With the Néel interaction Hamiltonian now fully defined, this model can be implemented into the SPIN package of LAMMPS, completing the desired magnetic model for the coupled SD-MD simulation tool. Moving forward, we see an opportunity to use the same procedure outline here to produce similar models of spin-orbit coupling in other HCP materials such as Gadolinium. Also, given the arbitrary nature of the DFT database needed to fit these models, we aim to also produce SOC functions of BCC materials such as Iron.

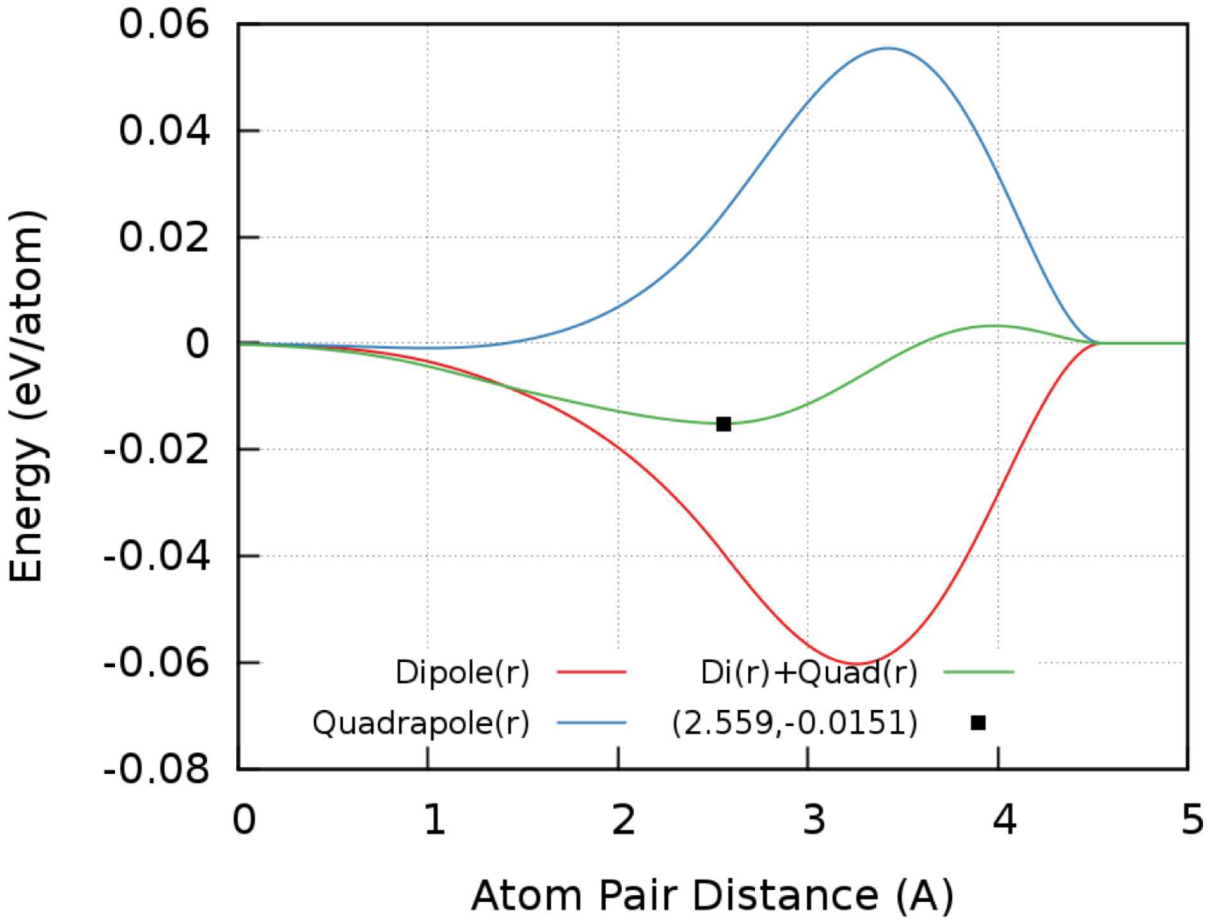

Figure 4.3: DAKOTA optimized spin orbit interaction functions. Each of the functions is a polynomial of order four with each of the coefficients taken as free variables during fitting. Single black point indicates the minima of the sum of dipolar and quadrapolar terms, this equilibrium distance is very close to the relaxed nearest neighbor distance of 2.49Å in HCP cobalt.

Chapter 5

Summary and Outlook

In the introduction, four limitations of existing coupled SD-MD implementation were discussed. This project allowed us to provide Sandia and the DOE with a new numerical tool tackling those four limitations.

Indeed, a scalable numerical tool allowing to perform coupled SD-MD simulations was released as a package in LAMMPS, and is now pubicly available. Two extensions of this first version of the SD-MD implementations were also presented in this report : models accounting for long-range magnetic dipolar interactions, and the developement and paramatrization of inter-atomic potentials accounting for spin-orbit coupling effects. Future publications will provide more details about those two developments.

This new numerical tool should be greatly beneficial to many ongoing and future projects at Sandia for the development of functional magnetic materials, such as tagging applications or quantum-computing devices.

Extending the impact of this new SD-MD tool will depend strongly on the available material models to interested users, the desired material specificity for these users comes down to the exchange and spin-orbit Hamiltonian terms. At the conclusion of this work, we have demonstrated to the broad audience of LAMMPS users a generalizable example of how one such spin-orbit coupling model can be developed and implemented.

This page intentionally left blank.

Appendix A

Poisson Bracket for Spin-Lattice Equations of Motions

The equations of motion (EOMs) and the magnetic and mechanical forces can be derived from the spin–lattice Hamiltonian. Yang *et al.* derived a generalized formulation of the Poisson bracket for spin–lattice systems [32]. With $f\left(t, \boldsymbol{r}_i, \boldsymbol{p}_i, \boldsymbol{s}_i\right)$ and $g\left(t, \boldsymbol{r}_i, \boldsymbol{p}_i, \boldsymbol{s}_i\right)$ two functions of time, position, momentum and spin :

$$\{f, g\} = \sum_{i=1}^{N} \left[\frac{\partial f}{\partial \boldsymbol{r}_i} \cdot \frac{\partial g}{\partial \boldsymbol{p}_i} - \frac{\partial f}{\partial \boldsymbol{p}_i} \cdot \frac{\partial g}{\partial \boldsymbol{r}_i} - \frac{\boldsymbol{s}_i}{\hbar} \cdot \left(\frac{\partial f}{\partial \boldsymbol{s}_i} \times \frac{\partial g}{\partial \boldsymbol{s}_i} \right) \right]. \tag{A.1}$$

Its application to a spin–lattice Hamiltonian $\mathcal{H}_{sl}$ (typically, the one defined by eq. (3.1) leads to the following set of EOMs for the spin–lattice system :

$$\frac{d\boldsymbol{r}_i}{dt} = \{\boldsymbol{r}_i, \mathcal{H}_{sl}\} = \frac{\boldsymbol{p}_i}{m_i} \tag{A.2}$$

$$\frac{d\boldsymbol{p}_i}{dt} = \{\boldsymbol{p}_i, \mathcal{H}_{sl}\} = \boldsymbol{F}_i \tag{A.3}$$

$$\frac{d\boldsymbol{s}_i}{dt} = \{\boldsymbol{s}_i, \mathcal{H}_{sl}\} = \boldsymbol{\omega}_i \times \boldsymbol{s}_i \tag{A.4}$$

where the mechanical force $\boldsymbol{F}_i$ is given by :

$$\boldsymbol{F}_i = -\frac{\partial \mathcal{H}_{sl}}{\partial \boldsymbol{r}_i} \tag{A.5}$$

and the magnetic precession vector $\boldsymbol{\omega}_i$ is given by :

$$\boldsymbol{\omega}_i = -\frac{1}{\hbar} \frac{\partial \mathcal{H}_{sl}}{\partial \boldsymbol{s}_i}. \tag{A.6}$$

This page intentionally left blank.

Appendix B

Sixth-Rank Magnetostriction Coefficients

In chapter 4, magnetostriction results were obtained from density functional theory calculations. This appendix aims at providing a bridge between those magnetostriction calculations to the radial functions $g(r)$ and $q(r)$ defined in eq. (4.1).

By following the work of Mason (up to the sixth rank magnetostriction tensor) [29] and combining it to the work of Bruno [33], the magnetostriction can be expressed as follows :

$$\begin{aligned}\lambda &= A\left[2\alpha_1\alpha_2\beta_1 + (\alpha_1-\alpha_2)^2\beta_2\right]^2 + B\alpha_3^2\left[(\alpha_1\beta_1+\alpha_2\beta_2)^2 - (\alpha_1\beta_2-\alpha_2\beta_1)^2\right] \\ &\quad + C\left[(\alpha_1\beta_1+\alpha_2\beta_2)^2 - (\alpha_1\beta_2+\alpha_2\beta_1)^2\right] + D\left(1-\alpha_3^2\right)\left(1-\beta_3^2\right) \\ &\quad + E\alpha_3^2\beta_3^2\left(1-\alpha_3^2\right) + F\alpha_3^2\left(1-\alpha_3^2\right) + G\beta_3^2\left(1-\alpha_3^2\right) \\ &\quad + H\alpha_3\beta_3\left(\alpha_1\beta_1+\alpha_2\beta_2\right) + I\alpha_3^3\beta_3\left(\alpha_1\beta_1+\alpha_2\beta_2\right) \end{aligned} \tag{B.1}$$

where $\boldsymbol{\alpha}$ is the direction of the averaged magnetization, and $\boldsymbol{\beta}$ is a unitary vector giving the direction in which the lattice strain is measured.

The nine magnetostriction coefficients (A to$I$) in eq. (B.1) can be expressed as functionals of $g(r)$ and $q(r)$, and are given by :

$$A = N_{222} - N_{111} \tag{B.2}$$
$$B = 3\left(N_{131} - N_{132} + N_{121}\right) + N_{111} - 2N_{222} \tag{B.3}$$
$$C = \left(2N_{222} - N_{111} - 3N_{121}\right) + \frac{1}{2}\left(M_{11} - M_{12}\right) \tag{B.4}$$
$$D = \left(2N_{111} - 2N_{222} + 3N_{121} - N_{331}\right) + \frac{1}{2}\left(M_{11} + M_{12} - 2M_{31}\right) \tag{B.5}$$
$$E = 2\left(N_{111} - N_{222}\right) + 3\left(N_{121} - N_{131} + N_{132} - N_{123}\right) + 6N_{133} + N_{331} - N_{333} \tag{B.6}$$
$$F = 2\left(N_{222} - N_{111}\right) - N_{331} + 3\left(N_{131} + N_{132} - N_{121}\right) + 6N_{133} + N_{331} - N_{333} \tag{B.7}$$
$$G = \left(3N_{123} - N_{333}\right) + \left(M_{13} - M_{33}\right) \tag{B.8}$$
$$H = 8N_{155} + 2M_{44} \tag{B.9}$$
$$I = 8\left(N_{344} - N_{155}\right) \tag{B.10}$$

where the M_{ij} and N_{ijk} coefficients are derived from the expression of the Néel pair anisotropy and geometric considerations associated to the hcp cell.

For the M_{ij} coefficients, one has the following expressions :

$$
\begin{aligned}
M_{11} &= \left(\tilde{S}_{11} - \tilde{S}_{1111}\right)\left(g(r) - \frac{6}{7}q(r)\right) + \frac{1}{2}\tilde{S}_{1111}\left(r\frac{\partial g}{\partial r} - \frac{6}{7}\frac{\partial q}{\partial r}\right) && \text{(B.11)}\\
M_{33} &= \left(\tilde{S}_{33} - \tilde{S}_{3333}\right)\left(g(r) - \frac{6}{7}q(r)\right) + \frac{1}{2}\tilde{S}_{3333}\left(r\frac{\partial g}{\partial r} - \frac{6}{7}\frac{\partial q}{\partial r}\right) && \text{(B.12)}\\
M_{12} &= \tilde{S}_{1122}\left(\frac{6}{7}q(r) - g(r) + \frac{1}{2}\left(r\frac{\partial g}{\partial r} - \frac{6}{7}\frac{\partial q}{\partial r}\right)\right) && \text{(B.13)}\\
M_{13} &= \tilde{S}_{1133}\left(\frac{6}{7}q(r) - g(r) + \frac{1}{2}\left(r\frac{\partial g}{\partial r} - \frac{6}{7}\frac{\partial q}{\partial r}\right)\right) && \text{(B.14)}\\
M_{31} &= M_{13} && \text{(B.15)}\\
M_{44} &= \left(\tilde{S}_{22} - 2\tilde{S}_{2233}\right)\left(g(r) - \frac{3}{7}q(r)\right) + \tilde{S}_{2233}\left(r\frac{\partial g}{\partial r} - \frac{6}{7}\frac{\partial q}{\partial r}\right) && \text{(B.16)}
\end{aligned}
$$

where $g(r)$ and $q(r)$ are the two radial functions associated to the Néel pair anisotropy (see eq. (4.1)), and the $\tilde{S}_{IJK}$ are geometric coefficients.

We now provide a definition for those geometric coefficients. The $\tilde{S}_{IJK}$ coefficients represent nearest neighbor shell (NN) sums, presenting 2 to 6 indices, and are evaluated according to the following expression :

$$\tilde{S}_{ijkl\ldots} = \sum_{NN} \beta_i\beta_j\beta_k\beta_l\ldots \qquad \text{(B.17)}$$

with $beta_i$ For symmetry reasons, the indices in $\tilde{S}_{ijkl\ldots}$ will always appear by pairs, and the Voigt notation system is used :

$$
\begin{aligned}
11 &\rightarrow 1,\ 22 \rightarrow 2,\ 33 \rightarrow 3,\\
23 &\rightarrow 4,\ 13 \rightarrow 5,\ 12 \rightarrow 6, && \text{(B.18)}
\end{aligned}
$$

reducing the number of indices in the $\tilde{S}$ coefficients from 2 to 6, to 1 to 3, respectively. Geometric considerations of the hcp lattice allow to evaluate (using trigonometric functions) the values of those coefficients. Table B.1 provides the values of all necessary $\tilde{S}$ coefficients.

Finally, the two tables below provide all the $Nijk$ coefficients (also as functionals of $g(r)$, $q(r)$, and the $\tilde{S}_{IJK}$ coefficients).

$\tilde{S}_1 = \tilde{S}_2 = \tilde{S}_3 = 4$	$\tilde{S}_{11} = \tilde{S}_{22} = \frac{5}{2}$
$\tilde{S}_{33} = \frac{8}{3}$	$\tilde{S}_{12} = \frac{5}{6}$
$\tilde{S}_{13} = \tilde{S}_{23} = \frac{2}{3}$	$\tilde{S}_{111} = \frac{17}{8}$
$\tilde{S}_{222} = \frac{127}{72}$	$\tilde{S}_{333} = \frac{16}{9}$
$\tilde{S}_{112} = \frac{5}{24}$	$\tilde{S}_{122} = \frac{41}{72}$
$\tilde{S}_{113} = \tilde{S}_{223} = \frac{1}{6}$	$\tilde{S}_{133} = \tilde{S}_{233} = \frac{4}{9}$
$\tilde{S}_{123} = \frac{1}{18}$	

Table B.1: Values of the second, fourth and sixth order $\tilde{S}_{ijkl..}$ coefficients.

$$N_{111} = 4q(r_{ij})\tilde{S}_{1111} + \left(r_{ij}\frac{\partial q}{\partial r_{ij}} - q(r_{ij})\right)\tilde{S}_{111111} \tag{B.19}$$

$$N_{112} = \left(r_{ij}\frac{\partial q}{\partial r_{ij}} - q(r_{ij})\right)\tilde{S}_{111122} \tag{B.20}$$

$$N_{121} = 2q(r_{ij})\tilde{S}_{1122} + \left(r_{ij}\frac{\partial q}{\partial r_{ij}} - q(r_{ij})\right)\tilde{S}_{111122} \tag{B.21}$$

$$N_{166} = \frac{1}{2}q(r_{ij})\left(\tilde{S}_{1111} + 3\tilde{S}_{1122}\right) + \left(r_{ij}\frac{\partial q}{\partial r_{ij}} - q(r_{ij})\right)\tilde{S}_{111122} \tag{B.22}$$

$$N_{221} = \left(r_{ij}\frac{\partial q}{\partial r_{ij}} - q(r_{ij})\right)\tilde{S}_{112222} \tag{B.23}$$

$$N_{122} = 2q(r_{ij})\tilde{S}_{1122} + \left(r_{ij}\frac{\partial q}{\partial r_{ij}} - q(r_{ij})\right)\tilde{S}_{112222} \tag{B.24}$$

$$N_{266} = \frac{1}{2}q(r_{ij})\left(\tilde{S}_{2222} + 3\tilde{S}_{1122}\right) + \left(r_{ij}\frac{\partial q}{\partial r_{ij}} - q(r_{ij})\right)\tilde{S}_{112222} \tag{B.25}$$

$$N_{113} = \left(r_{ij}\frac{\partial q}{\partial r_{ij}} - q(r_{ij})\right)\tilde{S}_{222233} \tag{B.26}$$

$$N_{131} = 2q(r_{ij})\tilde{S}_{1133} + \left(r_{ij}\frac{\partial q}{\partial r_{ij}} - q(r_{ij})\right)\tilde{S}_{111133} \tag{B.27}$$

$$N_{155} = \frac{1}{2}q(r_{ij})\left(\tilde{S}_{1111} + 3\tilde{S}_{1133}\right) + \left(r_{ij}\frac{\partial q}{\partial r_{ij}} - q(r_{ij})\right)\tilde{S}_{111133} \tag{B.28}$$

$$N_{331} = \left(r_{ij}\frac{\partial q}{\partial r_{ij}} - q(r_{ij})\right)\tilde{S}_{113333} \tag{B.29}$$

$$N_{133} = 2q(r_{ij})\tilde{S}_{1133} + \left(r_{ij}\frac{\partial q}{\partial r_{ij}} - q(r_{ij})\right)\tilde{S}_{113333} \tag{B.30}$$

$$N_{355} = \frac{1}{2}q(r_{ij})\left(\tilde{S}_{3333} + 3\tilde{S}_{1133}\right) + \left(r_{ij}\frac{\partial q}{\partial r_{ij}} - q(r_{ij})\right)\tilde{S}_{113333} \tag{B.31}$$

$$N_{223} = \left(r_{ij}\frac{\partial q}{\partial r_{ij}} - q(r_{ij})\right)\tilde{S}_{113333} \tag{B.32}$$

$$N_{232} = 2q(r_{ij})\tilde{S}_{2233}\left(r_{ij}\frac{\partial q}{\partial r_{ij}} - q(r_{ij})\right)\tilde{S}_{222233} \tag{B.33}$$

$$N_{244} = \frac{1}{2}q(r_{ij})\left(\tilde{S}_{2222} + 3\tilde{S}_{2233}\right) + \left(r_{ij}\frac{\partial q}{\partial r_{ij}} - q(r_{ij})\right)\tilde{S}_{222233} \quad \text{(B.34)}$$

$$N_{332} = \left(r_{ij}\frac{\partial q}{\partial r_{ij}} - q(r_{ij})\right)\tilde{S}_{223333} \quad \text{(B.35)}$$

$$N_{233} = 2q(r_{ij})\tilde{S}_{2233}\left(r_{ij}\frac{\partial q}{\partial r_{ij}} - q(r_{ij})\right)\tilde{S}_{223333} \quad \text{(B.36)}$$

$$N_{344} = \frac{1}{2}q(r_{ij})\left(\tilde{S}_{3333} + 3\tilde{S}_{2233}\right) + \left(r_{ij}\frac{\partial q}{\partial r_{ij}} - q(r_{ij})\right)\tilde{S}_{223333} \quad \text{(B.37)}$$

$$N_{123} = \left(r_{ij}\frac{\partial q}{\partial r_{ij}} - q(r_{ij})\right)\tilde{S}_{112233} \quad \text{(B.38)}$$

$$N_{132} = \left(r_{ij}\frac{\partial q}{\partial r_{ij}} - q(r_{ij})\right)\tilde{S}_{112233} \quad \text{(B.39)}$$

$$N_{231} = \left(r_{ij}\frac{\partial q}{\partial r_{ij}} - q(r_{ij})\right)\tilde{S}_{112233} \quad \text{(B.40)}$$

$$N_{144} = \frac{1}{2}q(r_{ij})\left(\tilde{S}_{1122} + \tilde{S}_{1133}\right) + \left(r_{ij}\frac{\partial q}{\partial r_{ij}} - q(r_{ij})\right)\tilde{S}_{112233} \quad \text{(B.41)}$$

$$N_{255} = \frac{1}{2}q(r_{ij})\left(\tilde{S}_{1122} + \tilde{S}_{2233}\right) + \left(r_{ij}\frac{\partial q}{\partial r_{ij}} - q(r_{ij})\right)\tilde{S}_{112233} \quad \text{(B.42)}$$

$$N_{366} = \frac{1}{2}q(r_{ij})\left(\tilde{S}_{1133} + \tilde{S}_{2233}\right) + \left(r_{ij}\frac{\partial q}{\partial r_{ij}} - q(r_{ij})\right)\tilde{S}_{112233} \quad \text{(B.43)}$$

$$N_{222} = 4q(r_{ij})\tilde{S}_{2222} + \left(r_{ij}\frac{\partial q}{\partial r_{ij}} - q(r_{ij})\right)\tilde{S}_{222222} \quad \text{(B.44)}$$

$$N_{333} = 4q(r_{ij})\tilde{S}_{3333} + \left(r_{ij}\frac{\partial q}{\partial r_{ij}} - q(r_{ij})\right)\tilde{S}_{333333} \quad \text{(B.45)}$$

In this appendix, we only provided the results, and do not detail the associated calculations. Future publication will provide more explanation about the associated analytical evaluation of those coefficients.

Appendix C

Magnetic Field Dependent Density of State Calculations using the Elk Code

This Appendix breifly reviews some of the calculations performed by Attila Cangi (org. 1444) using the Elk code [30].

Those calculations aimed at probing how the density of state (DoS) evolved for a magnetic system submitted to a large magnetic field (which can be the case in magnetostricition experiments). Figure C.1 below presents the obtained results.

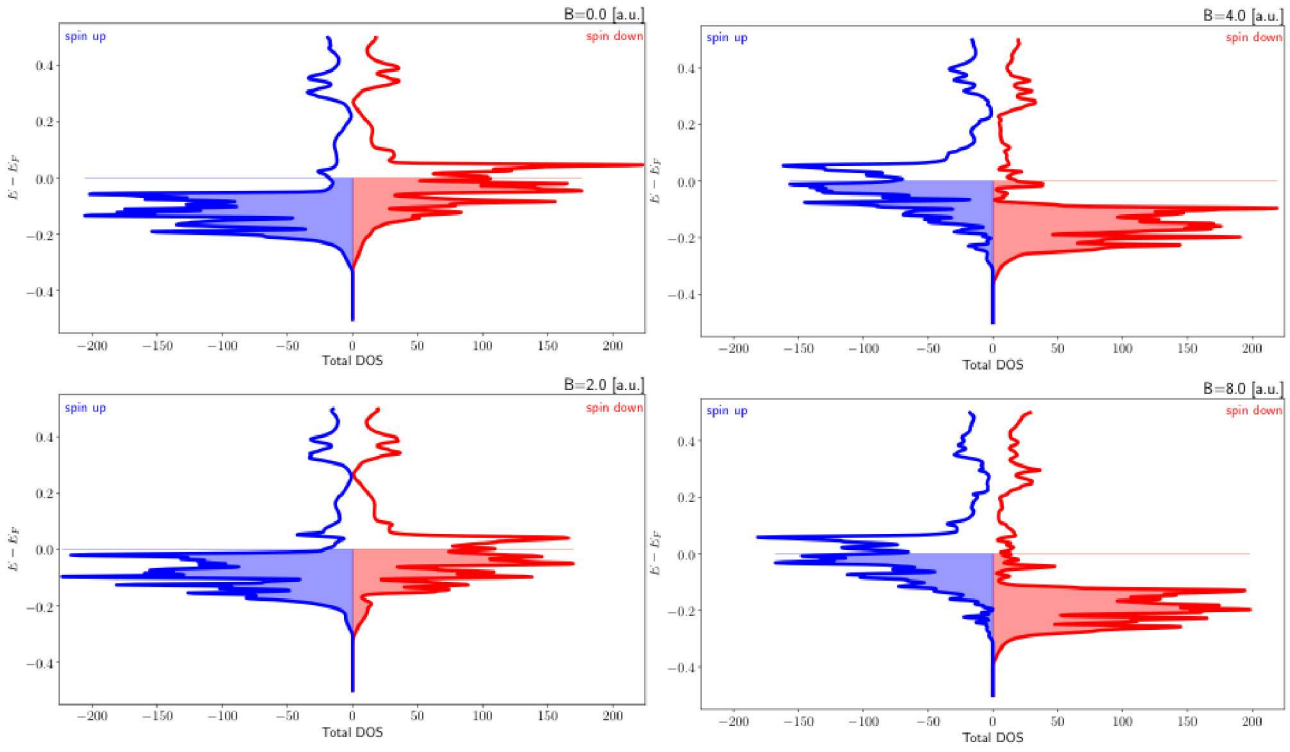

Figure C.1: Density of states plots for both spin-up (series in blue) and spin-down (series in red) channels calculated using Elk. Each panel represents a different magnetic field strength with the top-left panel being the DoS in the absence of an applied field. Above $4.7 \cdot 10^5$ T, shown in the right two panels, there is a significant change in the occupied states(shaded curves) with respect to the zero field DoS.

This page intentionally left blank.

Bibliography

[1] Daan Frenkel and Berend Smit. *Understanding molecular simulation: from algorithms to applications*, volume 1. Elsevier, 2001.

[2] Olle Eriksson, Anders Bergman, Lars Bergqvist, and Johan Hellsvik. *Atomistic spin dynamics: Foundations and Applications*. Oxford university press, 2017.

[3] VP Antropov, MI Katsnelson, BN Harmon, M Van Schilfgaarde, and D Kusnezov. Spin dynamics in magnets: Equation of motion and finite temperature effects. *Physical Review B*, 54(2):1019, 1996.

[4] Haohua Wen, Pui-Wai Ma, and CH Woo. Spin-lattice dynamics study of vacancy formation and migration in ferromagnetic bcc iron. *Journal of Nuclear Materials*, 440(1):428–434, 2013.

[5] Pui-Wai Ma and SL Dudarev. Dynamic magnetocaloric effect in bcc iron and hcp gadolinium. *Physical Review B*, 90(2):024425, 2014.

[6] Mark Mudrick, Markus Eisenbach, Dilina Perera, G Malcolm Stocks, and David P Landau. Combined molecular and spin dynamics simulation of bcc iron with lattice vacancies. In *Journal of Physics: Conference Series*, volume 921, page 012007. IOP Publishing, 2017.

[7] Pui-Wai Ma, SL Dudarev, and CH Woo. Spilady: A parallel cpu and gpu code for spin–lattice magnetic molecular dynamics simulations. *Computer Physics Communications*, 207:350–361, 2016.

[8] Dilina Perera, Don M Nicholson, Markus Eisenbach, G Malcolm Stocks, and David P Landau. Collective dynamics in atomistic models with coupled translational and spin degrees of freedom. *Physical Review B*, 95(1):014431, 2017.

[9] Dilina Perera, Markus Eisenbach, Don M Nicholson, G Malcolm Stocks, and David P Landau. Reinventing atomistic magnetic simulations with spin-orbit coupling. *Physical Review B*, 93(6):060402, 2016.

[10] Steve Plimpton. Fast parallel algorithms for short-range molecular dynamics. *Journal of computational physics*, 117(1):1–19, 1995.

[11] J Tranchida, SJ Plimpton, P Thibaudeau, and AP Thompson. Massively parallel symplectic algorithm for coupled magnetic spin dynamics and molecular dynamics. *Journal of Computational Physics*, 2018.

[12] Michael P Allen and Dominic J Tildesley. *Computer simulation of liquids*. Oxford university press, 2017.

[13] Zuowei Wang and Christian Holm. Estimate of the cutoff errors in the ewald summation for dipolar systems. *The Journal of Chemical Physics*, 115(14):6351–6359, 2001.

[14] Andrés Aguado and Paul A Madden. Ewald summation of electrostatic multipole interactions up to the quadrupolar level. *The Journal of chemical physics*, 119(14):7471–7483, 2003.

[15] Juan J Cerda, V Ballenegger, O Lenz, and Christian Holm. P^3M algorithm for dipolar interactions. *The Journal of chemical physics*, 129(23):234104, 2008.

[16] Abdulnour Toukmaji, Celeste Sagui, John Board, and Tom Darden. Efficient particle-mesh ewald based approach to fixed and induced dipolar interactions. *The Journal of chemical physics*, 113(24):10913–10927, 2000.

[17] Roger W Hockney and James W Eastwood. *Computer simulation using particles*. crc Press, 1988.

[18] Markus Deserno and Christian Holm. How to mesh up ewald sums. i. a theoretical and numerical comparison of various particle mesh routines. *The Journal of chemical physics*, 109(18):7678–7693, 1998.

[19] In-Chul Yeh and Max L Berkowitz. Ewald summation for systems with slab geometry. *The Journal of chemical physics*, 111(7):3155–3162, 1999.

[20] Louis Néel. L'approche à la saturation de la magnétostriction. *J. Phys. Radium*, 15(5):376–378, 1954.

[21] P Bruno. Magnetic surface anisotropy of cobalt and surface roughness effects within Neel's model. *J. Phys. F: Met. Phys.*, 18(6):1291–1298, June 1988.

[22] SM Foiles, MI Baskes, and Murray S Daw. Embedded-atom-method functions for the fcc metals cu, ag, au, ni, pd, pt, and their alloys. *Physical review B*, 33(12):7983, 1986.

[23] GP Purja Pun and Y Mishin. Embedded-atom potential for hcp and fcc cobalt. *Physical Review B*, 86(13):134116, 2012.

[24] Georg Kresse and Jürgen Hafner. Ab initio molecular dynamics for liquid metals. *Physical Review B*, 47(1):558, 1993.

[25] Georg Kresse and Jürgen Furthmüller. Efficient iterative schemes for ab initio total-energy calculations using a plane-wave basis set. *Physical review B*, 54(16):11169, 1996.

[26] Georg Kresse and Jürgen Furthmüller. Efficiency of ab-initio total energy calculations for metals and semiconductors using a plane-wave basis set. *Computational materials science*, 6(1):15–50, 1996.

[27] John P Perdew, Kieron Burke, and Matthias Ernzerhof. Generalized gradient approximation made simple. *Physical review letters*, 77(18):3865, 1996.

[28] SL Dudarev, GA Botton, SY Savrasov, CJ Humphreys, and AP Sutton. Electron-energy-loss spectra and the structural stability of nickel oxide: An LSDA+U study. *Physical Review B*, 57(3):1505, 1998.

[29] W.P. Mason. Derivation of magnetostriction and anisotropic energies for hexagonal, tetragonal, and orthorhombic crystals. *Phys. Rev.*, 96:302, 1954.

[30] Kay Dewhurst *et. al.* Elk Electronic Structure Code, 2018.

[31] Brian M Adams, WJ Bohnhoff, KR Dalbey, JP Eddy, MS Eldred, DM Gay, K Haskell, Patricia D Hough, and Laura P Swiler. Dakota, a multilevel parallel object-oriented framework for design optimization, parameter estimation, uncertainty quantification, and sensitivity analysis: version 5.0 user's manual. *Sandia National Laboratories, Tech. Rep. SAND2010-2183*, 2009.

[32] Kuo-Ho Yang and Joseph O Hirschfelder. Generalizations of classical Poisson brackets to include spin. *Physical Review A*, 22(5):1814, 1980.

[33] Patrick Bruno. Magnetic surface anisotropy of cobalt and surface roughness effects within neel's model. *Journal of Physics F: Metal Physics*, 18(6):1291, 1988.

DISTRIBUTION:

1	MS 1320	Scott S. Collis, 01440 (electronic copy)
1	MS 1321	Veena Tikare, 01444 (electronic copy)
1	MS 1322	Attila Cangi, 01444 (electronic copy)
1	MS 1322	Stan G. Moore, 01444 (electronic copy)
1	MS 1322	Steven J. Plimpton, 01444 (electronic copy)
1	MS 1322	Aidan P. Thompson, 01444 (electronic copy)
1	MS 1322	Julien Tranchida, 01444 (electronic copy)
1	MS 1322	Mitchell Wood, 01444 (electronic copy)
1	MS 0899	Technical Library, 9536 (electronic copy)
1	MS 0359	D. Chavez, LDRD Office, 1911

Sandia National Laboratories